Inorganic Chemistry

Article

pubs.acs.org/IC

Control of the Iridium Oxidation State in the Hollandite Iridate Solid Solution $K_{1-x}Ir_4O_8$

Artem Talanov,[†,‡] W. Adam Phelan,[†,‡] Zachary A. Kelly,[†] Maxime A. Siegler,[†] and Tyrel M. McQueen*[,†,‡]

[†]Department of Chemistry, and [‡]Department of Physics and Astronomy, Institute for Quantum Matter, Johns Hopkins University, Baltimore, Maryland 21218, United States

Supporting Information

ABSTRACT: The synthesis and physical properties of the $K_{1-x}Ir_4O_8$ ($0 \leq x \leq 0.7$) solid solution are reported. The structure of KIr_4O_8, solved with single-crystal X-ray diffraction at $T = 110$ K, is found to be tetragonal, space group $I4/m$, with $a = 10.0492(3)$ Å and $c = 3.14959(13)$ Å. A highly anisotropic displacement parameter is found for the potassium cation. Density functional theory calculations suggest that this anisotropy is due to a competition between atomic size and bond valence. KIr_4O_8 has a significant electronic contribution to the specific heat, $\gamma = 13.9$ mJ mol-Ir^{-1} K^{-2}, indicating an effective carrier mass of $m^*/m_e \approx 10$. Further, there is a magnetic-field-dependent upturn in the specific heat at $T < 3$ K, suggestive of a magnetically sensitive phase transition below $T < 1.8$ K. Resistivity and magnetization measurements show that both end-members of the solid solution, KIr_4O_8 and $K_{1-x}Ir_4O_8$ ($x \approx 0.7$), are metallic, with no significant trends in the temperature-independent contributions to the magnetization. These results are interpreted and discussed in the context of the importance of the variability of the oxidation state of iridium. The differences in physical properties between members of the $K_{1-x}Ir_4O_8$ ($0 \leq x \leq 0.7$) series are small and appear to be insensitive to the iridium oxidation state.

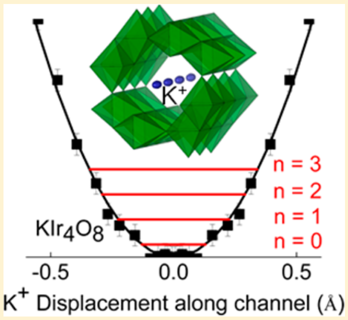

■ INTRODUCTION

Research on iridates has blossomed because of the similar energy scales of electron−electron repulsion (Hubbard U) and spin−orbit coupling (SOC). An array of electronic and magnetic behaviors occurs depending upon which term is more dominant. For example, Sr_2IrO_4 exhibits weak ferromagnetism below $T = 240$ K and anisotropic metallic resistance below $T = 120$ K,[1] while $BaIrO_3$ exhibits the formation of a charge density wave accompanying a ferromagnetic transition at $T_C = 180$ K.[2,3] Reducing the dimensionality has a profound effect, as the layered (2-D) honeycomb compounds A_2IrO_3 (A = Na/Li) are insulating, exhibit unusual magnetic orders, and may be close to a spin liquid regime.[4,5]

Further reducing the effective dimensionality to one dimension has the potential to produce interesting physical properties as well, as has been seen in systems such as the cuprates and the iron pnictides/chalcogenides.[6−9] Hollandites are a family of compounds with general formulas AB_4O_8 or AB_6O_{12} and a quasi 1-D (Q-1D) structure.[10] The structure consists of double-chains of edge-sharing BO_6 octahedra; adjacent double chains are connected at the corners and form large one-dimensional channels in which the *A* cations reside (see Figure 1). The connections between BO_6 octahedra create a Q-1D structure due to edge-sharing along the length of the double-chains and corner-sharing perpendicular to the double-chains. Further, some hollandites display variable occupancy for the *A* cations, such as $NaLi_2Ru_6O_{12}$[11] and KRu_4O_8,[12] suggesting the possibility of chemically charge doping the materials (often required to achieve the most interesting electronic behaviors[13]).

Hollandites accommodate various transition metals for the B cations, which in turn give rise to varying and interesting physical properties. For example, the series of 3d transition-metal oxide hollandites includes B = Ti, V, Cr, and Mn. These compounds display various unusual physical properties, including metal−insulator transitions in KCr_4O_8,[14] KV_4O_8,[15] and $Pb_{1.6}V_8O_{16}$;[16] spin-singlet formation in KV_4O_8;[17] ferromagnetism in KCr_4O_8;[18] and antiferromagnetism in $Pb_{1.6}V_8O_{16}$.[16] Additionally, the series of 4d transition-metal oxide hollandites, including B = Mo, Ru, and Rh, also displays interesting properties, including Q-1D conduction.[19] Most interestingly, $BaRu_6O_{12}$ shows a highly unusual temperature dependence of magnetic susceptibility and has a possible quantum phase transition near $T = 2$ K between a metallic state and a competing, weakly localized state, tunable by the disorder and magnetic field.[20]

In this work we report the structure of KIr_4O_8 based on single-crystal X-ray diffraction (XRD) and report its physical properties. It is the only currently known 5d transition metal hollandite,[21] and there are only scant reports on its physical properties. Further, we demonstrate the ability to tune the formal oxidation state of iridium by preparing the solid solution $K_{1-x}Ir_4O_8$ ($0 \leq x \leq 0.7$).

■ EXPERIMENTAL SECTION

Polycrystalline pellets and single crystals of KIr_4O_8 were obtained by heating ground, pelletized mixtures of dried K_2CO_3 (Alfa Aesar,

Received: January 22, 2014
Published: April 16, 2014

dx.doi.org/10.1021/ic5001667 | *Inorg. Chem.* 2014, 53, 4500−4507

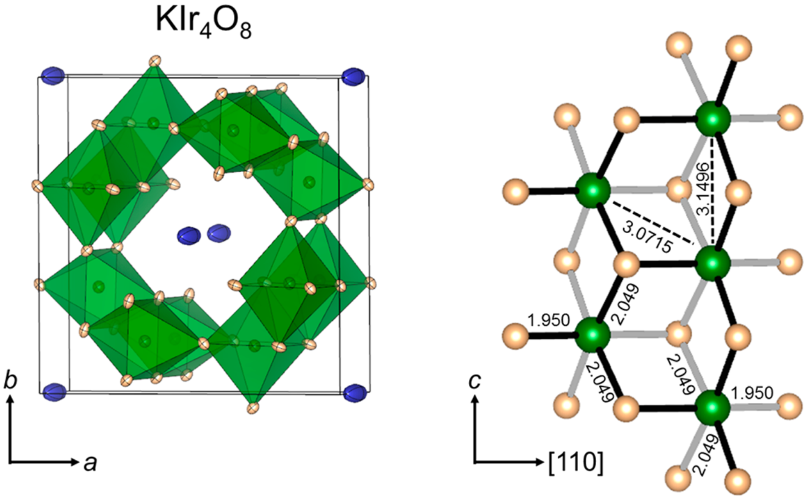

Figure 1. The structure of KIr_4O_8, built of potassium ions (blue) and IrO_6 octahedra (green and orange with green polyhedral shading). Potassium ions reside in the channels formed by double chains of the IrO_6 octahedra. A single double chain can be viewed as a one-dimensional cut out of a layer of edge-sharing IrO_6 octahedra. Select atom−atom distances are given in units of Å. (Errors are provided in Table 2.)

98.5%) and Ir black (J&J Materials, Inc.), with a 1:2 ratio of K/Ir, at 1123−1273 K for 4−15 h in capped alumina crucibles. The amount of K_2CO_3 used was double the stoichiometric amount to account for volatilization. Black/silver malleable single crystals in the shape of needles with the approximate size $1 \times 0.002 \times 0.002$ mm^3 were obtained from the surfaces of the pellet and from the inside surfaces of the crucible. In some cases, the formation of extremely thin crystals was observed after only 15 min of heating. The inside of the pellet was a black polycrystalline powder of KIr_4O_8. Similar reactions were attempted using IrO_2 (prepared by heating Ir black in air at 1273 K) instead of Ir black, as previously reported,[21,22] but these resulted in the volatilization of all of the K_2CO_3 leaving behind only IrO_2.

The deintercalation of potassium from KIr_4O_8 was performed by immersing the powders in 10 mL solutions of stoichiometric quantities of bromine in acetonitrile and stirring at room temperature for 3−5 days. Solid $K_{1-x}Ir_4O_8$ polycrystalline powders were recovered by decanting, rinsing, and centrifuging repeatedly and finally heat-drying. Samples of $K_{1-x}Ir_4O_8$ of targeted compositions $x = 0.15$, 0.3, 0.45, 0.6, and 0.75 were made. Deintercalated samples were stored in a desiccator. A deintercalated $K_{1-x}Ir_4O_8$ crystal was prepared by gluing a crystal to a glass slide and immersing it for a week in a 10 mL solution of acetonitrile containing an excess of bromine.

Laboratory powder XRD was performed using Cu Kα radiation on a Bruker D8 Focus diffractometer with a LynxEye detector. A Mo standard, with a lattice parameter of $a = 3.14737$ Å, was used in all samples to obtain accurate relative unit cell parameters. Le Bail refinements to extract the lattice parameters were performed in TOPAS (Bruker AXS). Scanning electron microscopy (SEM) and energy-dispersive X-ray spectroscopy (EDX) analyses were performed on a JEOL JSM-6700F field emission scanning electron microscope.

Single-crystal XRD was carried out by mounting a crystal of KIr_4O_8 on a loop with a tiny amount of Paratone-N oil. All reflection intensities were measured using a SuperNova diffractometer (equipped with an Atlas detector) with Mo Kα radiation ($\lambda = 0.71073$ Å) under the CrysAlisPro software suite (version 1.171.36.28, Agilent Technologies, 2012). CrysAlisPro was also used to index the cell dimensions and to perform data reduction. The temperature was fixed at $T = 110(2)$ K using the Cryojet system (manufactured by Oxford Instruments). The generation of the initial models and structure refinement were conducted using SIR97[23] and SHELXL-2013,[24] respectively. The tetragonal Laue symmetry $4/m$ and the observed systematic absences led to the space group selection of $I4/m$ (No. 87). After the refinement of all of the atomic positions, the collected data were corrected for absorption (i.e., a face-indexed analytical absorption correction was applied using CrysAlisPro). The displacement parameters were then refined as anisotropic and weighting schemes were applied during the final stages of refinement.

Density functional theory (DFT) calculations were performed using Elk[25] with the Perdew−Wang/Ceperley−Alder LDA functional[26] and the default full potential linearized augmented plane wave (FP-LAPW) basis set with local orbitals specified for K, Ir, and O. All calculations were performed on the experimentally determined reduced primitive unit cell, but with the symmetry lowered to $I4$ to allow for calculation of the total energy as a function of the potassium ion position along the channels. A $4 \times 2 \times 2$ k-point mesh was used and calculations were converged to better than 1.0×10^{-4} Ha in energy and 1.0×10^{-5} rms change in Kohn−Sham potential. Spin−orbit coupling was included. Convergence of all of the calculations was checked with respect to angular momentum cutoffs and the number of empty orbitals included.

The temperature dependence of the observed rate constant for the reaction $KIr_4O_8 + 0.25\ Br_2 \rightarrow K_{0.5}Ir_4O_8 + 0.5\ KBr$ was determined by monitoring the average reaction rate at different temperatures, as was previously done for $K_{1-x}Ni_2Se_2$.[13] A single starting batch of KIr_4O_8 was ground and divided into nine aliquots. The reactions were performed in a warm oil bath (309.8(5) K), at room temperature (296.2(3), 295.8(3), 295.6(3) K), in a refrigerator (275.0(3) K), in an ice water bath (273.2(3) K), in a freezer (250.3(3), 247.9(3) K), and in a bath containing ethanol/ethylene glycol with dry ice (236.7(3) K). The powders were placed into the respective reaction vessels, immersed in 1.00 mL of acetonitrile, and allowed to reach the correct temperatures. Once at temperature, 0.08 mL of concentrated bromine in acetonitrile was added to each reaction vessel. The reaction vessels were immediately returned to their respective environments to maintain temperature. For each reaction, the contents were not mixed. The reaction series was monitored visually, and each reaction was observed to go to completion when the solution turned from a pale yellow color to a colorless solution.

Magnetization, resistivity, and specific heat measurements were performed using a Physical Properties Measurement System (Quantum Design, Inc.). Electrical resistivity measurements were performed along the c-axis (long axis) of the needle-shaped single crystals using the four-probe method, where the platinum leads were mounted in a linear configuration onto the single crystals using silver epoxy. The contact and sample dimensions were obtained from SEM micrographs. Magnetization measurements were performed on the polycrystalline powders. Heat capacity measurements were performed on the sintered polycrystalline pieces using the semi-adiabatic pulse technique.

■ RESULTS AND DISCUSSION

Figure 2 shows a typical powder diffraction pattern for KIr_4O_8. KIr_4O_8 was previously reported to crystallize in the monoclinic space group $I2/m$, based on subtle peak splitting in the powder diffraction.[21] However, IrO_2 is a common impurity phase obtained in the preparation of KIr_4O_8 (see Figure 2 inset) and all of its major reflections in the range of 5° < 2θ < 60° overlap with the reflections of KIr_4O_8. Consequently, samples containing IrO_2 could be interpreted as having peak splitting of some Bragg reflections, which might indicate a lower symmetry. Further complicating the analysis of powder diffraction data is that the needle-like habit of KIr_4O_8 crystals within the polycrystalline powder results in significant preferred orientation and varying reflection intensities along different axial directions. This makes the phase fractions of KIr_4O_8 and IrO_2 difficult to determine from relative peak intensities alone.

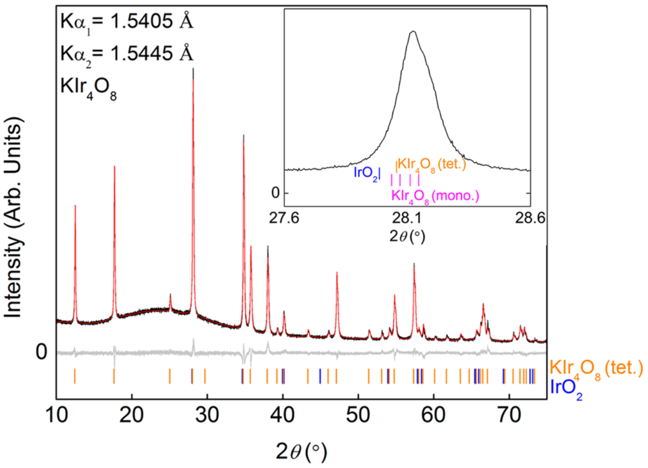

Figure 2. Rietveld refinement of room temperature powder X-ray diffraction data of KIr_4O_8 to the proposed tetragonal model. Inset: One Bragg reflection of KIr_4O_8, showing the overlap of a IrO_2 reflection which could be misinterpreted as a peak splitting arising from a monoclinic distortion of the KIr_4O_8 structure as previously reported.

Our single-crystal diffraction data collected at T = 110 K is consistent with either a $I2/m$ monoclinic cell with a unique angle of β = 89.993(4)°, or an $I4/m$ tetragonal cell. However, the unique monoclinic angle of the $I2/m$ cell is within 2σ of 90°, and it is closer to 90° than the previously determined angle of β = 90.113(3)°.[21] No evidence of peak splitting was observed in the single-crystal diffraction precession images or in our powder diffraction data (see Figure 2 inset). Additionally, the structure solutions in $I2/m$ and $I4/m$, when overlaid, are indistinguishable within error. Finally, the structure originally reported for KIr_4O_8[21] and the results from our monoclinic cell refinements were analyzed for extra symmetry elements using the program PLATON,[27] which determined that in both cases the symmetry should be changed from $I2/m$ to $I4/m$. Additional model refinements were conducted and models in $I4$ and $I\bar{4}$ were generated because $I4$, $I\bar{4}$, and $I4/m$ cannot be distinguished via systematic absences. E-statistics were used as guide to test for the presence of an inversion center. These statistics indicate that the choice of a centrosymmetric space group is favorable. Further, the oxygen atomic displacement parameters (ADPs) for the $I4$ and $I\bar{4}$ models refine to nonpositive definites, which can be a consequence of missed symmetry. Finally, the program Platon found missed or additional symmetry consistent with the $I4/m$ space group.

Although we cannot absolutely rule out a lower symmetry on a local scale, we assign tetragonal symmetry, space group $I4/m$, to KIr_4O_8 at T = 110 K. The crystallographic parameters and refinement details are listed in Table 1. The atomic coordinates, displacement parameters, and occupancies are listed in Table 2. Selected interatomic distances, angles, and bond valence sums are provided in Table 3. Least-squares analysis using isotropic ADPs yielded an R-value of 0.040, and analyses using anisotropic parameters yielded an R-value of 0.021. Allowing the potassium site occupancy to refine did not improve the refinement statistics.

Table 1. Final Crystallographic and Refinement Parameters for KIr_4O_8

Crystallographic Parameters	
a (Å)	10.0492(3)
c (Å)	3.14959(13)
V (Å^3)	318.07(2)
Z	2
cryst syst	tetragonal
space group	$I4/m$
θ range (deg)	4.0−40.7
μ (mm^{-1})	84.03
transm max	61.1%
transm min	6.4%
cryst habit	needle
size (mm)	0.148 × 0.008 × 0.006
Data Collection	
measured reflns	6659
independent reflns	558
reflns with $I > 2\sigma(I)$	517
R_{int}	0.064
h	−18 → 18
k	−18 → 18
l	−5 → 5
Refinement	
[a]R1[$F^2 > 2\sigma(F^2)$]; R1 [all data]	0.021; 0.024
[b]wR2(F^2)	0.042
params	21
GOF	1.08
$\Delta\rho_{max}$ (e Å^{-3})	3.48
$\Delta\rho_{min}$ (e Å^{-3})	−3.13

[a]R1 = $\sum||F_o| - |F_c||/\sum|F_o|$. [b]wR2 = $(\sum w(F_o^2 - F_c^2)^2/\sum w(F_o^2)^2)^{1/2}$.

The most unusual feature of the structural model is that the potassium cation ADPs show a high degree of anisotropy, where U_{33} is much higher than U_{11} and U_{22}. This was confirmed in a Fourier difference map, calculated by the subtraction of the data from a model that did not include the potassium ions, which showed the electron density around the K^+ sites to be very anisotropically spread out along the c-axis. No splitting of the crystallographic site was observed. A Hamilton R-ratio test was used to compare two models, one where the K ion was modeled on the 2b Wyckoff (ideal) site and one where the K ion was modeled on the 4e Wyckoff (split) site.[28] The split site model introduces one additional parameter but yields only a slight improvement in the wR2 quality of fit (4.16% vs 4.18%) that is not statistically significant at the 95% confidence level. Further, the displacement parameters remain significantly anisotropic even with the split

Table 2. Atomic Coordinates, Anisotropic Displacement Parameters, and Occupancies for KIr_4O_8 ($U_{12} = U_{23} = U_{31} = 0$)

atom	Wyckoff site	x	y	z	U_{11}	U_{22}	U_{33}	U_{eq} (Å^2)[a]
K1	2*b*	0	0	1/2	0.0214(13)	0.0214(13)	0.329(14)	0.124(5)
Ir1	8*h*	0.35113(2)	0.16640(2)	0	0.00544(19)	0.00533(9)	0.0278(8)	0.00452(2)
O1	8*h*	0.8042(2)	0.5451(4)	0	0.0094(17)	0.0066(15)	0.0038(14)	0.0066(6)
O2	8*h*	0.8484(4)	0.7968(4)	0	0.0063(16)	0.0071(16)	0.0039(14)	0.0058(6)

[a] U_{eq} is defined as $^1/_3$ of the trace of the orthogonalized U_{ij} tensor.

Table 3. Selected Interatomic Distances, Bond Valence Sums (BVS)[a], and Angles for KIr_4O_8

Distance (Å)	
K1–O1 (×8)	2.995(4)
Ir1–O1	1.950(4)
Ir1–O1 (×2)	1.995(3)
Ir1–O2	2.039(4)
Ir1–O2 (×2)	2.049(3)
Ir1–Ir1 (×2)	3.0715(3)
Ir1–Ir1 (×2)	3.1496(1)
BVS	
K1	+0.8
Ir1	+3.7
O1	−2.0
O2	−1.9
Angle (deg)	
O1–Ir1–O1 (×2)	91.9(2)
O1–Ir1–O1	104.28(19)
O1–Ir1–O2	171.52(17)
O1–Ir1–O2 (×2)	93.26(14)
O1–Ir1–O2 (×2)	92.01(15)
O1–Ir1–O2 (×2)	175.61(15)
O1–Ir1–O2 (×2)	77.50(13)
O2–Ir1–O2 (×2)	82.60(14)
O2–Ir1–O2	100.45(18)

[a] The BVS parameters used were as follows: K–O R_0 = 2.13;[45] Ir–O R_0 = 1.835 (calculated from the known structural parameters of IrO_2).[46] In all cases, a constant value of B = 0.37 was used.

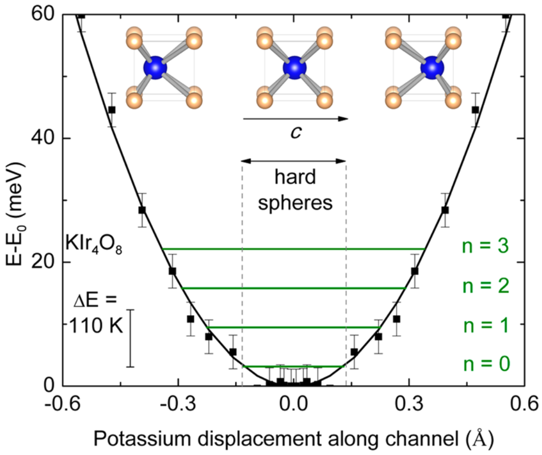

Figure 3. Results of the DFT calculations of the change in total energy versus the displacement of the potassium cation along the channel. The black line is a fit to a harmonic potential well, and the horizontal green lines indicate the first four allowed vibrational energy levels. Multiple excited vibrational states are accessible even at T = 110 K, resulting in significant movement of the potassium cations along the channels.

site model. Thus, we take the "ideal" model with potassium on the 2*b* site and the 8 equiv K–O bond lengths to be correct.

Similar ADP anisotropy of the A cations has been observed in other hollandites, including KRu_4O_8,[12] $Cs_{0.8}Li_{0.2}Ru_4O_8$,[10] and KV_4O_8;[29] however, such anisotropy is not universal, and others, such as KCr_4O_8,[30] do not show a large anisotropy. Yet others, such as $K_{1.33}Mn_8O_{16}$ and $Cs_{1.1}Ti_8O_{16}$, are best described by a split site model in which the A cations are displaced along the *c*-axis channels.[31,32] A number of explanations have been put forth to describe this behavior, including a dependence on the channel cation occupancy[29] or the relative ionic size of the cation to the channel. We performed DFT calculations of the total energy as a function of the channel potassium ion position to investigate the energies of potassium displacements in the case of KIr_4O_8. The results are shown in Figure 3. Up to potassium displacements of ~0.6 Å (0.16 relative lattice units along *c*), the change in energy is well described by a harmonic potential well with the form of $^1/_2kx^2$, where k is the bond force constant and x is the displacement. From this the angular frequency can be calculated through the relationship $\omega = (k/\mu)^{1/2}$ where μ is the reduced mass which, assuming the motion is dominated by the mass of a potassium ion, results in a characteristic frequency of $\omega = 9.60(13)\cdot 10^{12}$ Hz. The corresponding allowed vibrational energy levels for a harmonic oscillator are $E_n = \omega\hbar\cdot(n + {}^1/_2)$ where n is a non-negative integer, $\hbar$ is Planck's constant divided by 2π, and ω is the angular frequency. Given that $\omega = 9.60(13)\cdot 10^{12}$ Hz, the allowed vibrational energy levels are $E_n = 6.32(9)$ meV$\cdot(n + {}^1/_2)$. Even in the ground state ($n = 0$), the expected root mean square (rms) displacement of the potassium cations is predicted to be significant, ±0.1 Å ($= 0.15/\sqrt{2}$). Further, the first several excited modes are easily thermally accessed: even at T = 110 K, predicted vibrational populations are 0.25 ($n = 1$), 0.13 ($n = 2$), and 0.07 ($n = 3$); and the calculated rms displacement would be 0.36 Å. This was calculated by the following equation:

$$\sqrt{\langle Q^2\rangle} = \sum_{\nu=0}^{\infty}\sqrt{\frac{2\nu+1}{2\alpha}}\, e^{-\nu(h/2\pi)\omega}\left(1 - e^{-(h/2\pi)\omega}\right) \qquad \text{(a)}$$

This is substantially larger than is typical in solid state structures, and is in reasonable agreement with the $\sqrt{U_{33}}$ = 0.57 Å rms displacement that was actually observed for potassium along the length of the channels.

BVS calculated for KIr_4O_8 and the ionic radii suggest an explanation for this flat and broad energy surface: the potassium channel cation, which is coordinated by an O_8 cube, has BVS = 0.80, which is substantially less than the ideal value of 1.0 and implies that it is underbonded (Table 3). This is in contrast to the iridium, whose bond valence sum of +3.72 is close to the expected value of +3.75. Since the K—O distances are longer than the sum of their ionic radii, the potassium can move along the channel toward one face of the O_8 cube without experiencing significant core–core repulsion. This allows for an increase in its bonding to oxygen and BVS closer to unity (charge neutrality). The result is a very shallow potential well (in principle it is a slight double well, but our calculations did not show this feature, likely due to insufficient energy resolution) that allows for substantial motion along the channel direction and produces a highly anisotropic ADP for potassium. The competition between these two effects, local charge neutrality and atomic size, likely also explains why ADPs are sometimes isotropic and often anisotropic, while other times the *A* cation site splits into two: if the BVS energy gain outweighs the core−core repulsion sufficiently to produce a double-well potential, then a split site results.

The wide potential well calculated for the potassium cations leads to a lower transition state energy between sites, allowing for deintercalation using *chimie douce* techniques at room temperature. The overall chemical transformation, using bromine as an oxidant and deintercalation reagent, is $KIr_4^{3.75}O_8 + xBr_2 \rightarrow K_{1-2x}Ir_4^{3.75+x/2}O_8 + 2xKBr$. Figure 4 shows the resulting systematic change in the unit cell parameters. As more potassium is deintercalated, the *a*-lattice parameter increases, and the *c*-lattice parameter decreases. For all samples except for nominal $x = 0.75$, the characteristic yellow color of bromine disappeared from the acetonitrile solutions, indicating complete reactions. The lattice parameters changed linearly with the potassium content and follow Vegard's law.[33]

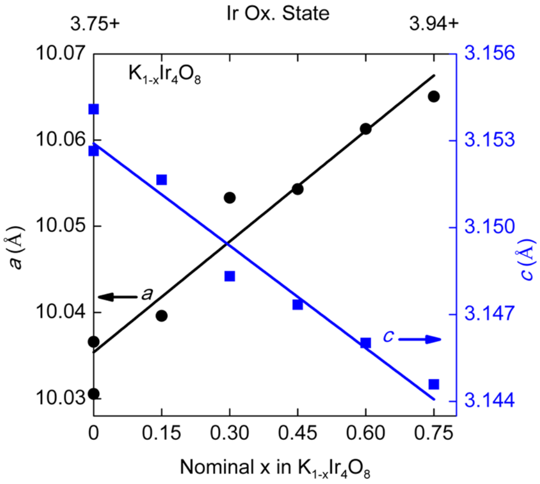

Figure 4. *a* and *c*-lattice parameters for KIr_4O_8 as a function of potassium concentration. The potassium content was targeted with bromine deintercalation. Statistical error bars are contained within the symbols. Lines guide the eye.

To understand the kinetics of the deintercalation reaction, the average reaction rate was measured for a single reaction performed at different temperatures with otherwise identical conditions. The logarithms of the resulting observed rate constants were plotted versus the inverse temperature (Figure 5) to obtain the average activation barrier of the rate-limiting step, calculated by using the Arrhenius relationship, $\ln(k_{avg}) = \ln(A) - (\Delta G^{\ddagger}/k_B)\ (1/T)$, where k_{avg} is the observed rate constant, A is the pre-exponential factor, $\Delta G^{\ddagger}$ is the activation barrier, k_B is the Boltzmann constant, and T is temperature. The average activation barrier using this method was determined to be 60(10) meV. This value is an order of magnitude smaller than the activation energy predicted by our DFT calculations (463(3) meV). This is not unexpected for two reasons. First, the DFT calculations are expected to overpredict the activation barrier since the surrounding oxygen lattice was not allowed to deform.[34,35] Second, the DFT calculations also assumed that all neighboring potassium sites were occupied, resulting in significant Coulombic repulsion between adjacent potassium cations. The observed value is a weighted average barrier during the course of transforming KIr_4O_8 to $K_{0.5}Ir_4O_8$; as potassium is removed, there is a greater concentration of vacancies. This reduces the energy barrier to deintercalate as the reaction proceeds since the potassium cations can move into a neighboring vacancy without experiencing Coulombic repulsion. Our measured value is in good agreement with the 32 meV activation barrier found in a related titanium hollandite with a fraction of alkali cation vacancies.[34,35]

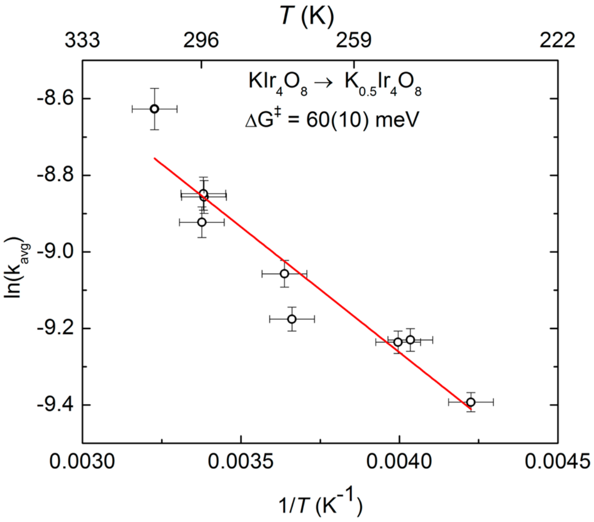

Figure 5. Temperature dependence of the observed rate constant (k_{avg}), linearized using the Arrhenius relationship, $\ln(k_{avg}) = \ln(A) - (\Delta G^{\ddagger}/k_B)\ (1/T)$, to determine the activation barrier, $\Delta G^{\ddagger}$, for $KIr_4O_8 + 0.25Br_2 \rightarrow K_{0.5}Ir_4O_8 + 0.5KBr$. $\Delta G^{\ddagger}$ = 60(10) meV.

The temperature-dependent magnetization data for $K_{1-x}Ir_4O_8$ are shown in Figure 6. All samples exhibit a paramagnetic upturn at low temperature that is well-modeled by the Curie−Weiss Law, $\chi = \chi_0 + C/(T - \theta_w)$, where χ_0 is the temperature-independent contribution, C is the Curie constant,

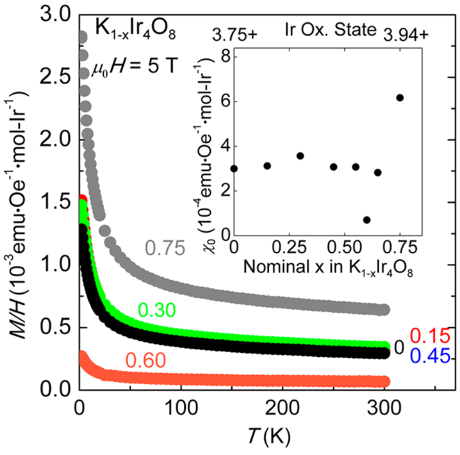

Figure 6. Susceptibility measurements of $K_{1-x}Ir_4O_8$ vs temperature, for various values of x. The data for x = 0.15 and 0.45 are overlapped by the data for x = 0 and 0.3. Inset: temperature-independent contributions (χ_0) for $K_{1-x}Ir_4O_8$, for various values of x, showing no systematic trend.

and θ_w is the Weiss temperature. Plots of $1/(\chi - \chi_0)$ versus T were made for low temperatures up to about 100 K, and values for χ_0 were chosen in order to achieve the most linear fit regions. Values for C and θ_w were then extracted from the linear fits and are given in Table 4. The values of C for $K_{1-x}Ir_4O_8$ range from 0.0071 to 0.0832 emu·K/Oe·mol-Ir. These small values imply that the Curie–Weiss contribution to the magnetic susceptibility is likely caused by orphan spins (0.375 is expected if it were due to one $S = 1/2$ spin per Ir ion) or small amounts of undetected secondary phase(s) instead of being intrinsic to $K_xIr_4O_8$. The temperature-independent susceptibility is on the order of 10^{-3}–10^{-4} emu/Oe/mol Ir, which is consistent with temperature-independent Pauli paramagnetism (TIPM). However, such susceptibility is larger than that of typical metals, and comparable to that found in other iridates, such as $Ba_2Ir_3O_9$, which has a TIPM contribution of 2.9×10^{-4} emu/Oe/mol Ir.[36] Similar magnetic behavior is also observed in the 4d ruthenate hollandites; however, the susceptibility of the ruthenate hollandites increases slightly with increases in temperature for $T > 100$ K.[10] KIr_4O_8 does not show this behavior.

Table 4. C and θ_w, Obtained from Linear Fits of $1/(\chi - \chi_0)$ vs T, for $K_{1-x}Ir_4O_8$ for Various Values of x

nominal x in $K_{1-x}Ir_4O_8$	C (emu·K·Oe^{-1}·mol-Ir^{-1})	θ_w (K)
0	0.0379(11)	−7.8(6)
0.15	0.0484(12)	−7.9(5)
0.3	0.0462(12)	−6.9(5)
0.45	0.0413(12)	−6.4(6)
0.6	0.0071(6)	−6.4(3)
0.75 (∼0.7)	0.083(4)	−6.6(9)

Resistivity data of KIr_4O_8 along the c-axis, shown in Figure 7, demonstrate that it is a good metallic conductor, with a residual resistivity ratio ($\rho_{300\ K}/\rho_{2K}$) (RRR) of 16.6 and $\rho_{2K} = 24$ $\mu\Omega$·cm. The RRR is a factor of 2–5 lower than that found for isomorphic KRu_4O_8, and the residual resistivity is an order of magnitude higher.[10,37] Resistivity measurements of the deintercalated $K_{1-x}Ir_4O_8$ crystal along the c-axis demonstrate that it is also a good metallic conductor, with a RRR of 9.6 and $\rho_{2K} = 53$ $\mu\Omega$·cm. A decrease in the RRR is expected due to the introduction of disorder upon the removal of the K ions. The estimated error in the absolute values of the resistivities is about ±20%. For $T < 60$ K, the resistivity is proportional to $T^{2.45}$, as shown in the inset in Figure 7. This power law, $\rho \propto T^n$ with $2 \leq n \leq 3$, is characteristic of electron–electron Umklapp scattering in quasi-one-dimensional (Q1D) conductors.[38] A similar power law behavior is also observed for the Q1D hollandites KRu_4O_8 ($T^{2.7}$)[37] and $Ba_{0.6}Rh_4O_8$ ($T^{2.5}$);[39] however, below about $T < 7$ K, the resistivity begins to fall below the $T^{2.45}$ proportionality.

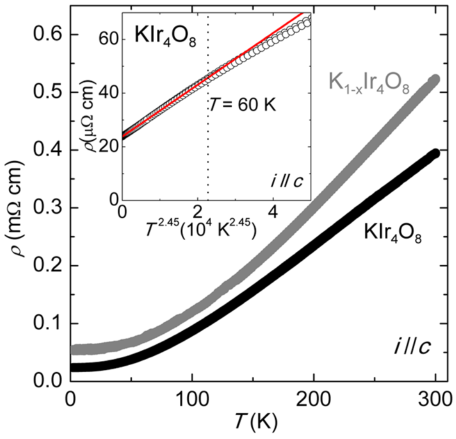

Figure 7. Temperature-dependent resistivity of KIr_4O_8 and $K_{1-x}Ir_4O_8$ ($x \approx 0.7$). The error bars on the exact resistivity values are about ±20% due to uncertainties in measuring the crystal dimensions. The inset shows that the resistivity data are well described by the power law, $\rho \propto T^n$ with $2 \leq n \leq 3$ below 60 K (dashed line). Deviation from this electron–electron Umklapp scattering is seen above the dashed line.

Figure 8 shows the specific heat capacity of KIr_4O_8 with applied magnetic fields of $\mu_0H = 0$ T and $\mu_0H = 5$ T. A plot of C/T versus T^2 should be linear at low temperatures if there are only conduction electron (T-linear) and lattice (T-cubed) contributions present, $C/T = \gamma + \beta_3T^2$. A linear region exists below 13 K for both of the applied fields. For $\mu_0H = 0$ T, the heat capacity deviates below $T < 3.3$ K; a linear best-fit line to the data, fit in the linear range of $3.3\ K < T < 13.1$ K, is shown. For $\mu_0H = 5$ T, the heat capacity deviates for $T < 5.0$ K. A linear best-fit line to the data, fit in the linear range of $5.0\ K < T < 13.1$ K, is shown. From the best-fit line for the zero-field data, the Sommerfeld parameter γ, characterizing the electronic contribution to the specific heat, is given by $\gamma = 13.9$ mJ/(mol-Ir K^2), which is considerably larger than the value reported for KRu_4O_8, $\gamma = 3$ mJ/(mol-Ru K^2).[10] In KIr_4O_8, the electron count is between Ir^{3+} (d^6) and Ir^{4+} (d^5). Assuming there is one hole carrier per iridium ion (as would be expected for low spin d^5), the expected Sommerfeld contribution is only ∼1.2 mJ/(mol-Ir K^2). This implies that the carriers in KIr_4O_8 have a significant effective mass, ∼10 times that of a free electron. The slope of this best-fit line gives a Debye temperature of $\theta_D = 255$ K, a reasonable value for a quasi-low dimensional oxide.

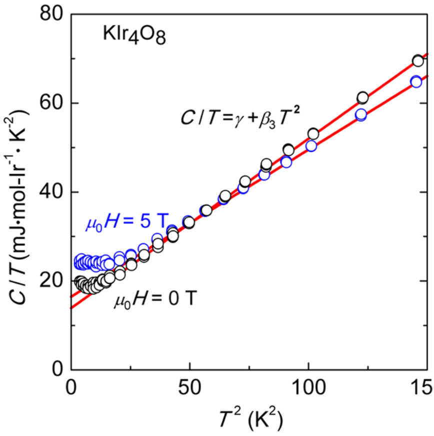

Figure 8. Specific heat normalized by temperature vs the square of temperature for KIr_4O_8. The $\mu_0H = 0$ T straight line (red) is fit to the region $3.3\ K < T < 13.1$ K; the $\mu_0H = 5$ T straight line (black) is fit to the region $5.0\ K < T < 13.1$ K.

The corresponding parameters for the $\mu_0H = 5$ T data are $\gamma = 16.5$ mJ/(mol–Ir K^2) and $\theta_D = 291$ K. The presence of the magnetic field influences both γ and β_3; however, this is unexpected because the lattice contribution should not be field dependent. Therefore, the change in β_3 signifies that there must be a magnetic field-dependent contribution (e.g., spin fluctuations or magnetic ordering).

The upturn in the specific heat below $T \approx 3.3$ K indicates a possible phase transition below our lowest measured temperature. This low-temperature behavior is consistent with the ordering of nuclear magnetic moments, or perhaps a more intriguing possibility would be an a quantum phase transition, like that found in $BaRu_6O_{12}$, which occurs around a similar temperature and is tunable by the magnetic field.[20] It is too large to originate from possible undetected secondary phases. Measurements below 1.9 K are necessary to understand this behavior.

Except for in oxides, iridium in oxidation states above 3+ are rare due to the high stability of the low spin d^6 in an octahedral crystal field. Recent calculations have shown that the Ir^{4+} (d^5) electronic configuration becomes stabilized in oxides due to the effects of spin−orbit coupling.[40] It is thus interesting to speculate that effects of spin−orbit coupling may be responsible for the enhanced low-temperature specific heat of this material.

■ CONCLUSION

The structure of KIr_4O_8 was analyzed by single-crystal XRD and was determined to be tetragonal, rather than monoclinic as it was previously reported.[21] Deintercalation of the potassium ion resulted in a systematic shift in the lattice parameters. The controlled removal of potassium cations systematically varied the formal iridium oxidation state from +3.75 ($x = 0$) to +3.93 ($x = 0.7$) in $K_{1-x}Ir_4O_8$. Previous researchers have prepared oxides with intermediate valence iridium (e.g., $Pb_2Ir_2O_{6.5-x}$, Li_xIrO_2, $Bi_2Ir_2O_{7-y}$, and $BaIrO_{3-\delta}$),[41−44] but there are scant reports of the systematic variability of the iridium oxidation state in single phase materials. Magnetization measurements for KIr_4O_8 and $K_{1-x}Ir_4O_8$ show temperature-independent Pauli paramagnetism with a small Curie tail, likely due to orphan spins. Resistivity shows metallic temperature dependence with residual resistivity ratios of 16.6 and 9.6 for the KIr_4O_8 and $K_{1-x}Ir_4O_8$ crystals, respectively. Heat capacity measurements for KIr_4O_8 show a heat contribution that is neither lattice nor electronic below 3.3 K for a 0 T magnetic field and below 5 K for a 5 T field. Further heat capacity measurements below 1.9 K are necessary in order to understand the origin of this extra contribution. More generally, we have shown that it is possible to systematically and precisely control the Ir^{3+}/Ir^{4+} ratio in an extended oxide, and we have provided an explanation for the highly anisotropic thermal parameters found in many hollandites.

■ ASSOCIATED CONTENT

Ⓢ Supporting Information

XRD results for KIr_4O_8 are available in the form of a crystallographic information file (CIF). This material is available free of charge via the Internet at http://pubs.acs.org.

■ AUTHOR INFORMATION

Corresponding Author

*E-mail: mcqueen@jhu.edu.

Notes

The authors declare no competing financial interest.

■ ACKNOWLEDGMENTS

The authors acknowledge Mark Koontz of the Materials Science and Engineering Department at the Johns Hopkins University for facilitating the use of the SEM instrument. T.M.M. acknowledges the donors of the American Chemical Society Petroleum Research Fund and the National Science Foundation (NSF), Division of Materials Research (DMR), CAREER Grant No. 1253562. Finally, W.A.P. acknowledges Benjamin A. Trump for useful discussions with regard to the heat capacity measurements.

■ REFERENCES

(1) Cao, G.; Bolivar, J.; McCall, S.; Crow, J. E.; Guertin, R. P. *Phys. Rev. B: Condens. Matter* **1998**, *57*, 11039−11042.

(2) Nakano, T.; Terasaki, I. *Phys. Rev. B: Condens. Matter* **2006**, *73*, 195106.

(3) Cao, G.; Crow, J. E.; Guertin, R. P.; Henning, P. F.; Homes, C. C.; Strongin, M.; Basov, D. N.; Lochner, E. *Solid State Commun.* **2000**, *113*, 657−662.

(4) Singh, Y.; Manni, S.; Reuther, J.; Berlijn, T.; Thomale, R.; Ku, W.; Trebst, S.; Gegenwart, P. *Phys. Rev. Lett.* **2012**, *108*, 127203.

(5) Singh, Y.; Gegenwart, P. *Phys. Rev. B: Condens. Matter* **2010**, *82*, 064412.

(6) Abbamonte, P.; Blumberg, G.; Rusydi, A.; Gozar, A.; Evans, P. G.; Siegrist, T.; Venema, L.; Eisaki, H.; Isaacs, E. D.; Sawatzky, G. A. *Nature* **2004**, *431*, 1078−1081.

(7) Caron, J. M.; Neilson, J. R.; Miller, D. C.; Llobet, A.; McQueen, T. M. *Phys. Rev. B: Condens. Matter* **2011**, *84*, 180409.

(8) Caron, J. M.; Neilson, J. R.; Miller, D. C.; Arpino, K.; Llobet, A.; McQueen, T. M. *Phys. Rev. B: Condens. Matter* **2012**, *85*, 180405.

(9) Kamihara, Y.; Watanabe, T.; Hirano, M.; Hosono, H. *J. Am. Chem. Soc.* **2008**, *130*, 3296−3297.

(10) Foo, M. L.; Lee, W.-L.; Siegrist, T.; Lawes, G.; Ramirez, A. P.; Ong, N. P.; Cava, R. J. *Mater. Res. Bull.* **2004**, *39*, 1663−1670.

(11) Foo, M. L.; He, T.; Huang, Q.; Zandbergen, H. W.; Siegrist, T.; Lawes, G.; Ramirez, A. P.; Cava, R. J. *J. Solid State Chem.* **2006**, *179*, 941−948.

(12) Djafri, F.; Canonne, J.; Abraham, F.; Thomas, D. *J. Less-Common Met.* **1985**, *109*, 323−329.

(13) Neilson, J. R.; McQueen, T. M. *J. Am. Chem. Soc.* **2012**, *134*, 7750−7757.

(14) Hasegawa, K.; Isobe, M.; Yamauchi, T.; Ueda, H.; Yamaura, J.-I.; Gotou, H.; Yagi, T.; Sato, H.; Ueda, Y. *Phys. Rev. Lett.* **2009**, *103*, 146403.

(15) Isobe, M.; Koishi, S.; Kouno, N.; Yamaura, J.-I.; Yamauchi, T.; Ueda, H.; Gotou, H.; Yagi, T.; Ueda, Y. *J. Phys. Soc. Jpn.* **2006**, *75*, 073801.

(16) Maignan, A.; Lebedev, O. I.; Van Tendeloo, G.; Martin, C.; Hébert, S. *Phys. Rev. B: Condens. Matter* **2010**, *82*, 035122.

(17) Shimizu, Y.; Okai, K.; Itoh, M.; Isobe, M.; Yamaura, J.-I.; Yamauchi, T.; Ueda, Y. *Phys. Rev. B: Condens. Matter* **2011**, *83*, 155111.

(18) Endo, T.; Kume, S.; Kinomura, N.; Koizumi, M. *Mater. Res. Bull.* **1976**, *11*, 609−614.

(19) Ohta, Y.; Toriyama, T.; Sakamaki, M.; Konishi, T. *J. Phys.: Conf. Ser.* **2012**, *400*, 032070.

(20) Mao, Z. Q.; He, T.; Rosario, M. M.; Nelson, K. D.; Okuno, D.; Ueland, B.; Deac, I. G.; Schiffer, P.; Liu, Y.; Cava, R. J. *Phys. Rev. Lett.* **2003**, *90*, 186601.

(21) Bestaoui, N.; Deniard, P.; Brec, R. *J. Solid State Chem.* **1995**, *118*, 372−377.

(22) Ramírez, E.; Chavira, E.; Baños, L.; Soto Guzmán, A. B.; Guzmán, J.; Flores, C. *NSTI Nanotech 2006, NSTI Nanotechnol. Conf. Trade Show* **2006**, *1*, 830−833.

(23) Altomare, A.; Burla, M. C.; Camalli, M.; Cascarano, G. L.; Giacovazzo, C.; Guagliardi, A.; Moliterni, A. G. G.; Polidori, G.; Spagna, R. *J. Appl. Crystallogr.* **1999**, *32*, 115−119.

(24) Sheldrick, G. M. *Acta Crystallogr., Sect. A: Found. Crystallogr.* **2008**, *64*, 112−122.

(25) *The Elk FP-LAPW Code.* http://elk.sourceforge.net/ (accessed Aug 23, 2013).

(26) Perdew, J. P.; Wang, Y. *Phys. Rev. B: Condens. Matter* **1992**, *45*, 13244−13249.

(27) Spek, A. L. *Acta Crystallogr., Sect. D: Biol. Crystallogr.* **2009**, *65*, 148−155.

(28) Hamilton, W. C. *Acta Crystallogr.* **1965**, *18*, 502−510.

(29) Abriel, W.; Rau, F.; Range, K.-J. *Mater. Res. Bull.* **1979**, *14*, 1463−1468.

(30) Tamada, O.; Yamamoto, N.; Mori, T.; Endo, T. *J. Solid State Chem.* **1996**, *126*, 1−6.

(31) Vicat, J.; Fanchon, E.; Strobel, P.; Qui, D. T. *Acta Crystallogr., Sect. B: Struct. Sci.* **1986**, *42*, 162−167.

(32) Fanchon, E.; Hodeau, J. L.; Vicat, J.; Watts, J. A. *J. Solid State Chem.* **1991**, *92*, 88−100.

(33) Denton, A. R.; Ashcroft, N. W. *Phys. Rev. A* **1991**, *43*, 3161−3164.

(34) Geisel, T. *Phys. Rev. B: Condens. Matter* **1979**, *20*, 4294−4302.

(35) Weber, H.-P.; Schulz, H. *J. Chem. Phys.* **1986**, *85*, 475−484.

(36) Kawamura, Y.; Sato, H. *J. Alloys Compd.* **2004**, *383*, 209−212.

(37) Kobayashi, W. *Phys. Rev. B: Condens. Matter* **2009**, *79*, 155116.

(38) Oshiyama, A.; Nakao, K.; Kamimura, H. *J. Phys. Soc. Jpn.* **1978**, *45*, 1136−1146.

(39) Kobayashi, W.; Hébert, S.; Pérez, O.; Pelloquin, D.; Maignan, A. *Phys. Rev. B: Condens. Matter* **2009**, *79*, 085207.

(40) Miao, M.-S.; Seshadri, R. *J. Phys.: Condens. Matter* **2012**, *24*, 215503.

(41) Sleight, A. W. *Mater. Res. Bull.* **1971**, *6*, 775−780.

(42) Davidson, I. J.; Greedan, J. E. *J. Solid State Chem.* **1984**, *51*, 104−117.

(43) Kennedy, B. J. *J. Solid State Chem.* **1995**, *119*, 254−259.

(44) Powell, A. V.; Battle, P. D. *J. Alloys Compd.* **1996**, *232*, 147−153.

(45) Brese, N. E.; O'Keeffe, M. *Acta Crystallogr.* **1991**, *47*, 192−197.

(46) Bolzan, A. A.; Fong, C.; Kennedy, B. J.; Howard, C. J. *Acta Crystallogr.* **1997**, *53*, 373−380.